AGU PUBLICATIONS

JGR

Journal of Geophysical Research: Oceans

RESEARCH ARTICLE
10.1002/2015JC010782

Surface roughness and breaking wave properties retrieved from polarimetric microwave radar backscattering

Paul A. Hwang[1] and Franco Fois[2]

[1]Remote Sensing Division, Naval Research Laboratory, Washington, District of Columbia, USA, [2]Department of Geoscience and Remote Sensing, Delft University of Technology, Delft, Netherlands

Key Points:
- Roughness and breaking contributions of radar returns vary with polarization
- *VV* is dominated by roughness, *HH* and *VH* contain breaking information
- Breaking contributions depend on wind speed, frequency, and incidence angle

Correspondence to:
P. A. Hwang,
paul.hwang@nrl.navy.mil

Citation:
Hwang, P. A., and F. Fois (2015), Surface roughness and breaking wave properties retrieved from polarimetric microwave radar backscattering, *J. Geophys. Res. Oceans*, *120*, 3640–3657, doi:10.1002/2015JC010782.

Received 11 FEB 2015
Accepted 6 APR 2015
Accepted article online 10 APR 2015
Published online 23 MAY 2015

Abstract Ocean surface roughness and wave breaking are the two main contributors of radar backscattering from the ocean surface. The relative weightings of the two contributions vary with the microwave polarization: the *VV* (vertical transmit vertical receive) is dominated by the Bragg resonance scattering mechanism, and the *HH* (horizontal transmit horizontal receive) and *VH* (horizontal transmit vertical receive or vertical transmit horizontal receive) contain nontrivial non-Bragg contributions mainly produced by breaking features. A method is developed to obtain the short-scale properties of ocean surface roughness and wave breaking from Ku, C, and L band polarimetric sea returns. The results are used for quantitative evaluation of the ocean surface roughness spectral models and for deriving understanding of the breaking contribution important to microwave ocean remote sensing, in particular its dependence on wind speed, microwave frequency, and incidence angle. Implications of the results to air-sea interaction applications are discussed.

1. Introduction

Ocean surface roughness and surface wave breaking are two common factors important to the studies of ocean remote sensing and air-sea interaction. For example, remote sensing of the ocean surface vector wind by microwave radars and radiometers relies on the property that the normalized radar cross section (NRCS) and the sea surface brightness temperature are modified by the surface roughness and wave breaking and that the two oceanographic parameters are strongly influenced by the wind. For air-sea interaction processes such as gas transfer and sea spray aerosol generation, the boundary layer turbulence properties are closely associated with the surface roughness, and wave breaking represents a dominant source of turbulence generation and air entrainment in the upper ocean layer.

It is difficult to obtain quantitative measurements of surface roughness and wave breaking using conventional oceanographic instruments, especially in high-wind and high-wave conditions. Over the years, airborne and spaceborne scatterometers and polarimetric synthetic aperture radars (SARs) have produced a large amount of data for the construction of copolarized (*VV* and *HH*) and cross-polarized (*VH*) geophysical model functions (GMFs) with a broad coverage of wind speed ranging from mild to hurricane conditions. Because the response of microwave backscattering to the sea surface condition depends on the polarization, here we explore an empirical approach to derive the surface roughness and wave breaking information using the polarimetric differences of radar sea returns.

Presently, there are many GMFs for several microwave frequency bands: Ku, X, C, and L. Most of them are for copolarized returns *VV* and *HH*. Only the L and C bands offer several versions of the *VH* GMF [*Meissner et al*., 2014; *van Zadelhoff et al*., 2014; *Zhang et al*., 2014; *Hwang et al*., 2015]. In principle, they can all be used for our task of inferring the surface roughness and wave breaking properties.

In the following, we describe the approach in section 2. Results obtained from using Ku, C, and L band radar data are presented in section 3. The implication of roughness and breaking results on ocean surface processes, issues of different versions of GMFs, and computational efficiency are discussed in section 4 and a summary is given in section 5.

2. Approach

2.1. The General Concept

The GMFs are treated as proxies of global ocean data of surface roughness and wave breaking reflected on the radar backscattering through the interaction between microwave and the ocean surface. Three broad-category components are important contributors to the NRCS: (i) scattering from the tilted surface roughness component in Bragg resonance with the radar waves; (ii) the non-Bragg scattering from bubble plume features and discrete steep waveforms associated with wave breaking occurrences; and (iii) the modification of the relative permittivity from air entrained by wave breaking. Based on this classification, wave breaking causes three main changes: relative permittivity, surface roughness in the Bragg resonance portion, and non-Bragg scattering from bubble features and steep surface geometry.

Extensive studies have established that the *VV* is dominated by Bragg resonance scattering [e.g., *Wright*, 1966, 1968; *Valenzuela*, 1978; *Plant*, 1990]; therefore, it is most useful for understanding the ocean surface roughness properties. The surface roughness reflected in the *VV* sea returns includes both components of direct wind generation and breaking disturbances. In many practical applications of radar backscattering and air-sea interaction, the distinction of the generation sources is immaterial. For our purpose, the resultant from both generation sources is classified simply as the surface roughness. The *HH* and *VH* have higher degrees of breaking contributions from non-Bragg scattering mechanisms that are dependent on frequency, incidence angle, and wind speed.

We propose to use the second-order small slope approximation solution (SSA2) [*Voronovich*, 1994] to compute the Bragg resonance roughness contributions of *VV*, *HH*, and *VH*. The difference between GMFs and SSA2 solutions can then be used to construct an empirical model of breaking wave contributions relevant to radar backscattering. The version of the SSA2 solution described in *Fois et al*. [2014] is used in this work. In the case that the GMF is available for copolarized returns only, we also explore the composite-surface (or tilted) Bragg scattering solution (CB) [e.g., *Valenzuela*, 1978; *Plant*, 1990], which is computationally much more efficient than the SSA2 (about 1:800 ratio). The version of the CB solution described in *Hwang et al*. [2010] is used in this study.

In essence, we treat the GMFs as the sum of Bragg and non-Bragg contributions, corresponding to the roughness and breaking contributions classified in this paper. Using the property that *VV*, *HH*, and *VH* have different proportions of the two contributions, we attempt to sort out the two by comparing the GMFs with the analytical solutions of the Bragg contributions in *VV*, *HH*, and *VH*. This can be expressed symbolically as

$$\begin{aligned}\sigma_{0pq}(f,\theta,U_{10}) &= G_{pq}(f,\theta,U_{10})[B_R(k,U_{10})+B_B(\theta,k,U_{10})]\\ &= \sigma_{0Rpq}+\sigma_{0Bpq},\end{aligned} \tag{1}$$

where σ_0 is the NRCS, subscripts p and q are polarizations and can be either H or V, G_{pq} is the scattering coefficient, B_R is the dimensionless surface roughness spectrum, B_B is the breaking contribution expressed as an equivalent roughness spectrum, f is microwave frequency, θ is incidence angle, U_{10} is reference wind speed, and k is surface wave wave number. Due to the dominance of Bragg scattering, k is basically the Bragg resonance surface wave component k_B, which is related to the radar wave number k_e by $k_B = k_e 2\sin\theta$, therefore, k is a function of f andθ. The modification of the relative permittivity from air entrained by wave breaking impacts the scattering coefficient so G_{pq} is a function of f, θ, and U_{10}. Further discussion of (1) is deferred to section 3.1 after the presentation of the modifications of relative permittivity (section 2.3) and surface roughness spectrum (section 2.4).

The GMF established from global scattering measurements provides the total NRCS—the left-hand side of (1), and the SSA2 or CB solution provides the roughness contribution—the first term on the right-hand side. The difference between the two thus gives us the important information of the breaking contribution. It is recognized that the NRCS is also dependent on the azimuth angle ϕ (the radar pointing direction with respect to the wind direction). However, the fidelity of the directional distribution of roughness spectral models is questionable. For example, one of the most frequently used spectrum model for microwave computations is the E spectrum [*Elfouhaily et al*., 1997]. The directional distribution of the E spectrum is given by

$$D(\phi) = [1+B_2\cos(2\phi)]/2\pi, \tag{2}$$

with

$$B_2(k)=\tanh\left[a_0+a_p\left(\frac{c}{c_p}\right)^{2.5}+a_m\left(\frac{c_m}{c}\right)^{2.5}\right]$$
$$a_0=\frac{\ln 2}{4},\ a_p=4,\ a_m=0.13\frac{u_*}{c},\ c_m=\left(\frac{2g}{k_m}\right)^{0.5}=0.23\text{m/s}, \quad (3)$$

where u_* is the wind friction velocity, c is the phase speed of wave component with wave number k, subscript m represents the wave component with minimal phase speed, and subscript p is the wave spectral peak component. As discussed in section 1, the *VV* NRCS is dominated by the resonant Bragg scattering and we can use the *VV* GMF to investigate the directional distribution of the ocean surface roughness. The directional distributions of GMFs are typically expressed as

$$D(\phi)=[1+B_1\cos(\phi)+B_2\cos(2\phi)]/2\pi. \quad (4)$$

Figure 1 compares the B_2 coefficients based on the E spectral model and the CMOD5.n GMF [*Hersbach et al*., 2007; *Verspeek et al*., 2010] and Ku2001 GMF provided by Remote Sensing Systems (D. Smith, personal communication, 2009), showing large discrepancies between the model and observations. Because the method described in this paper for quantifying the surface roughness and breaking properties relies on the difference between GMFs and model computations, it is judged that the directional resolution of the model computation is not reliable at this stage. We are currently investigating the directional distribution issue. The result will be reported in a future paper.

2.2. Baseline Case

Here we illustrate as an example using the C band co- and cross-polarization GMFs for our analysis. The *VV* is based on CMOD5.n. The *HH* uses the CMOD5.n combined with the *VV/HH* polarization ratio, with the wind speed and incidence angle dependence established with the RADARSAT-2 (R2) quad-polarization data and the directional distribution of *Mouche et al*. [2005]; the detail is described in *Hwang et al*. [2010, Appendix A2]. The *VH* is from the empirical GMF established with dual-polarization (*VV*, *VH*) R2 wide-swath data with collocated buoy, stepped frequency microwave radiometer (SFMR), and H*Wind data sources from 19 hurricane wind scenes [*Zhang et al*., 2014; *van Zadelhoff et al*., 2014]; the detail is described in *Hwang et al*. [2015].

The NRCS based on the GMFs, computed for U_{10} between 3 and 60 m/s and θ between 20 and 50°, are shown in Figure 2a. As mentioned earlier, among these three polarizations, *HH* and *VH* are more sensitive to wave breaking in relative terms referenced to the Bragg scattering component. This is especially the case at high incidence angles, where scattering from Bragg resonance surface waves is very small. The wave breaking effects are less visible in *VV* because of the high Bragg contribution. Although our computations extend to 60 m/s, it is understood that the quality and quantity of high wind data used in the formulation and verification of GMFs are still evolving. Issues such as the drag coefficient relating the wind friction velocity and reference wind velocity are also troublesome in the high-wind region. However, the approach described here can be adapted to the improved GMFs in the future without major modification.

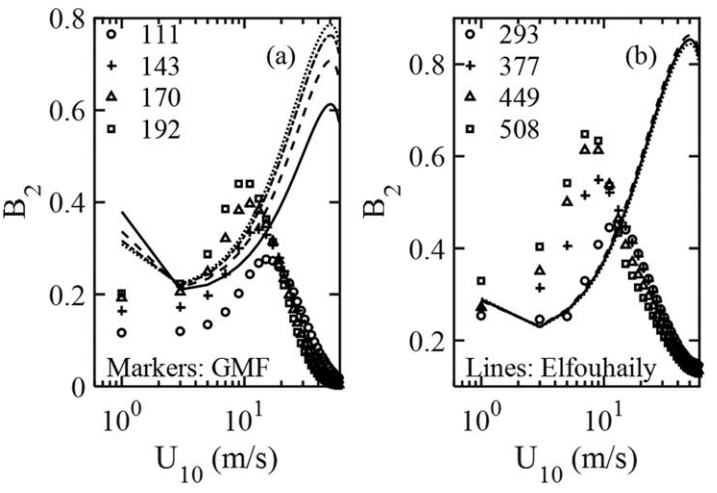

Figure 1. Comparison of the E spectrum directional distribution coefficient B_2 [*Elfouhaily et al*., 1997] with that obtained from (a) CMOD5.n GMF and (b) Ku2001 GMF. The incidence angles used in the computation are 20, 30, 40, and 50°. The corresponding Bragg wave numbers are illustrated in the legends.

As a baseline reference, the SSA2 solutions without

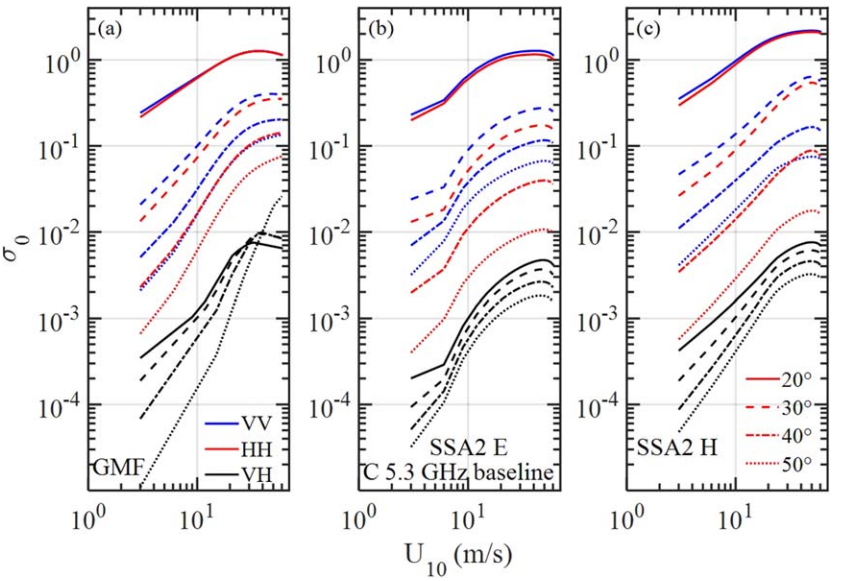

Figure 2. (a) C-band GMFs for *VV*, *HH*, and *VH* used in this study; (b) SSA2 solutions for *VV*, *HH*, and *VH* using the E roughness spectrum [*Elfouhaily et al*., 1997]; and (c) SSA2 solutions for *VV*, *HH*, and *VH* using the H roughness spectrum [*Hwang et al*., 2013].

considering the relative permittivity modification by foam are calculated using the published E (Figure 2b) and H (Figure 2c) roughness spectra: E for *Elfouhaily et al*. [1997] and H for *Hwang et al*. [2013]. The H spectral model includes swell influence, qualitatively increasing from 1 to 4. The results shown in Figure 2c represent mild swell influence (H2), close to the average of all the data used in the formulation of the H spectrum. The H spectrum is 1-D and can be coupled with various designs of the directional distribution function. To be consistent, the spreading function of the E spectrum is used for the H spectrum in this analysis. Both spectral models require the specification of friction velocity u_* as a function of the reference wind speed U_{10}. There are currently many different formulas of the drag coefficient C_{10} connecting u_* and U_{10}. In the present installation, we use the same formula discussed in *Hwang et al*. [2013] for both spectral models

$$C_{10}=10^{-5}\left(-0.16U_{10}^2+9.67U_{10}+80.58\right). \tag{5}$$

Figure 3 shows the NRCS ratio $\delta\sigma_{0pq}$ between the GMF and SSA2 solutions (GMF/SSA2) in dB values. A negative value means that the SSA2 solution is larger than the GMF value. Our basic assumption is that the GMF is the sum of contributions from roughness and wave breaking, and the SSA2 is the roughness contribution alone. When the GMF is less than SSA2, then either the roughness contribution is overestimated or the breaking contribution is negative. The former indicates overspecifying the Bragg-scale surface roughness. The latter can be from modification of the relative permittivity by the breaking entrained air. The air causes a decrease of the effective relative permittivity and thus reduces backscattering as a result of decreased reflectivity (section 2.3).

The *VV* is dominated by Bragg resonance scattering; therefore, it is especially useful for evaluating the roughness spectral models. For the baseline computations (Figures 3a–3c), the SSA2 solutions using the H spectral model are larger than the GMF in low and moderate winds ($U_{10}\leq\sim$12 m/s) for the whole range of incidence angles shown (20–50°), and at $\theta=20$ and 30° across the full range of wind speeds. This would indicate an overspecification of the Bragg resonance roughness spectral components. For the C band computations shown here, the Bragg wave numbers are 76, 111, 143, and 170 rad/m for the four incidence angles 20, 30, 40, and 50°, respectively. The SSA2 *VV* solutions of the baseline computations using the E spectrum is in excellent agreement with the GMF at $\theta=20°$. For 30–50°, the difference increases toward higher incidence angles.

To further address the discrepancy between the Bragg solutions and the GMFs, the relative permittivity modification by the breaking entrained air needs to be implemented. The difference between the SSA2 solution and the *VV* GMF can then provide some guideline for the roughness model refinement. The

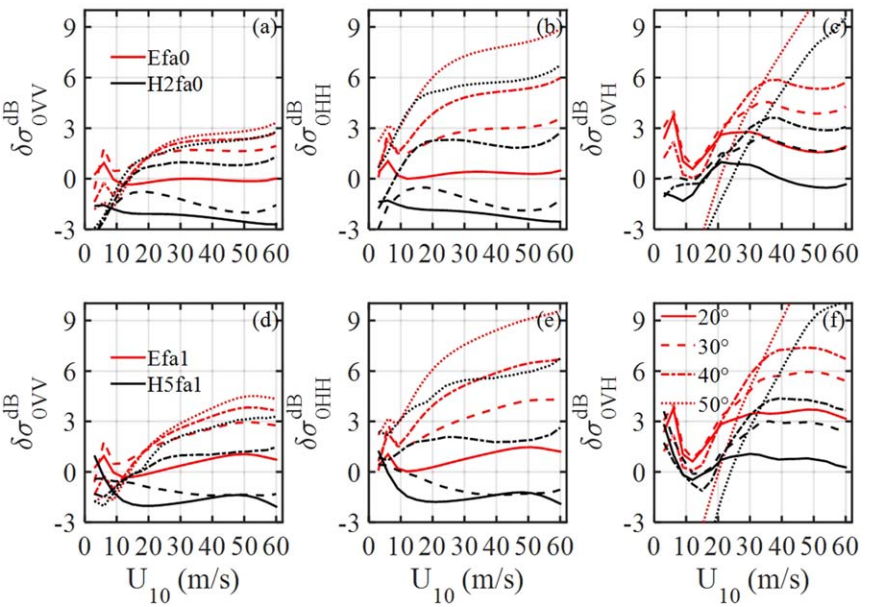

Figure 3. The ratio GMF/SSA2 (C band). (top row) the baseline computations without considering relative permittivity modification by foam: (a) *VV*, (b) *HH*, and (c) *VH*; results for E and H spectra are displayed; (bottom row) the corresponding results after including the modifications of relative permittivity and H roughness spectrum discussed in sections 2.3 and 2.4, respectively.

procedures to modify the relative permittivity and roughness spectral model are discussed next (sections 2.3 and 2.4). In the bottom row of Figure 3 we present a preview of the resulting $\delta\sigma_{0pq}$ following the implementation of the two modifications. There is a general improvement in the *VV* computed with the refined H spectrum, particularly in the lower wind regime. (The two versions of the H spectrum model are referred to as H13 and H15 when distinction is necessary.) A procedure to retrieve the breaking information using the resulting $\delta\sigma_{0HH}$ and $\delta\sigma_{0VH}$ is discussed in section 3.1.

2.3. Modification of the Relative Permittivity

For the relative permittivity modification, an equivalent medium approach using the mixing rule as described in *Hwang* [2012] is adapted. The relative permittivity differs significantly in air and in water for microwave frequencies; therefore, even a small amount of air can produce a large change in the relative permittivity of the resulting mixture. To account for the effect of entrained air, ideally we need to know the fraction of air in water (void fraction) and the vertical distribution of the bubble clouds carrying the air into water.

Considering the lack of such detailed oceanographic information of bubble cloud distribution and the small penetration depth of microwaves—for example, the skin depth is about 2 mm at 10 GHz [*Plant*, 1990]—*Hwang* [2012] uses the fraction of whitecap coverage as a proxy of the void fraction in the mixing rule for the evaluation of an effective relative permittivity ε_e. The approach renders the problem of ocean emission of foamy water from 3-D to 2-D (horizontal). The whitecap fraction represents an upper bound of the void fraction because it is equivalent to assuming 100% of air in the depth of microwave influence under the foamy area, whereas the actual air entrainment decreases exponentially with water depth [e.g., *Wu*, 1981; *Hwang et al*., 1990]. The effective relative permittivity ε_e of the air-water mixture is computed with the quadratic mixing rule in a similar way as discussed in *Anguelova* [2008]

$$\varepsilon_e = \left[f_a \varepsilon_a^{1/2} + (1 - f_a) \varepsilon_{sw}^{1/2} \right]^2, \tag{6}$$

where ε_{sw} is the relative permittivity of seawater without whitecaps, $\varepsilon_a = 1$ is the relative permittivity of air, and f_a is the air fraction approximated by the whitecap fraction.

Following the analysis presented in *Hwang* [2012], the formula for f_a is parameterized with the friction velocity u_* using the whitecap data reported in *Callaghan et al*. [2008]:

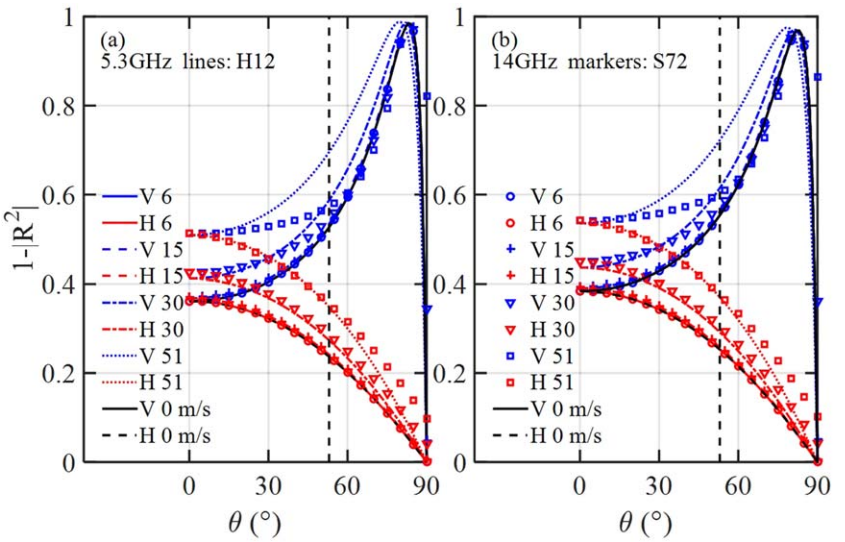

Figure 4. Comparison of the emissivity of a flat surface covered with foam from wave breaking, computed with the equivalent medium approach of *Hwang* [2012]: H12 (lines), and the formula by *Stogryn* [1972]: S72 (markers). The second column in the legend is wind speed in m/s. (a) C band 5.3 GHz and (b) Ku band 14 GHz.

$$f_a = \begin{cases} 0, & u_* \le 0.11\,\mathrm{m/s} \\ 0.30(u_* - 0.11)^3, & 0.11 < u_* \le 0.40\,\mathrm{m/s} \\ 0.07u_*^{2.5}, & u_* > 0.40\,\mathrm{m/s} \end{cases}. \tag{7}$$

The emissivity calculated by $1 - |R^2|$ with the "equivalent medium" relative permittivity produces similar results as that using the mixing rule applied to the emissivity of foamless sea surface area and the emissivity of 100%-foam area as treated in *Stogryn* [1972] for the *H* polarization but the two solutions differ significantly for the *V* polarization in high winds ($|R^2|$ is the Fresnel reflection coefficient). Figure 4 shows examples of emissivity computed for C and Ku bands using the two algorithms for several wind speeds between 0 and 51 m/s. The results of *Hwang* [2012] (labeled H12) are shown with continuous lines and the results of *Stogryn* [1972] (labeled S72) are shown with markers.

The calculated brightness temperature as a function of wind speed based on the equivalent medium approach is in very good agreement with a global data set of WindSat microwave radiometer measurements with wind speed coverage up to about 42 m/s [*Meissner and Wentz*, 2009]. The WindSat measurements include five microwave frequencies (6, 10, 18, 23, and 37 GHz) for both vertical and horizontal polarizations, and the nominal incidence angle is 53° (marked with a vertical dashed line in Figure 4) [see

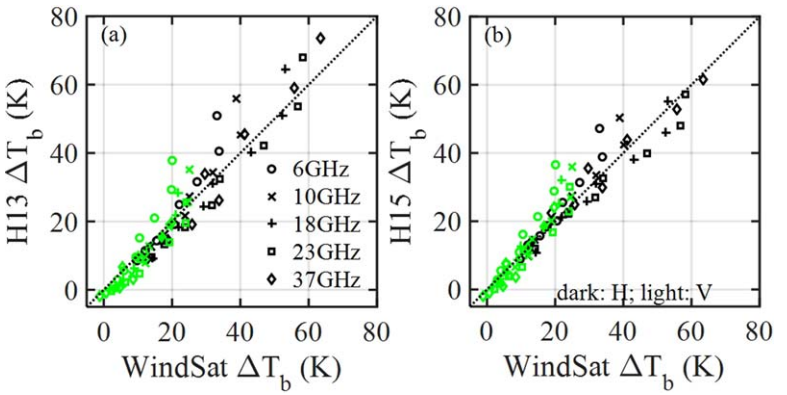

Figure 5. Comparison of wind-induced brightness temperature computed with emissivity modification treated by the equivalent medium approach of *Hwang* [2012] and (a) the roughness model of *Hwang et al.* [2013], labeled H13; and (b) the modified roughness model described in section 2.4, labeled H15.

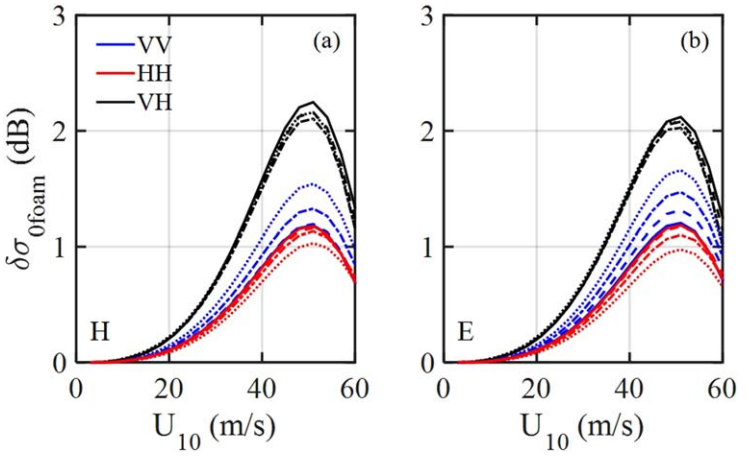

Figure 6. The impact on the C band NRCS computation by the foam modification of the relative permittivity; results are shown for (a) H spectrum and (b) E spectrum.

Hwang, 2012, Figure 3; *Hwang et al*., 2013, Figure 9]. Figure 5 shows the scatterplots of the observed wind-induced brightness temperature ΔT_b with that computed with the equivalent medium approach [*Hwang*, 2012], the results based on two versions of the H spectra are illustrated: (a) for *Hwang et al*. [2013]: H13, and (b) for the modified model described in section 2.4: H15. The statistics of bias, slope of linear regression, root mean squares (RMS) difference, and correlation coefficient for the two sets of calculations are (0.025 K, 1.07, 5.42 K, 0.96) for the former and (0.74 K, 1.04, 4.46 K, 0.96) for the latter. The total number of data population is 80.

Incorporating the foam-modified relative permittivity, the computed NRCS is always smaller than that without considering the modification as a result of decreased Fresnel reflection coefficients. Figure 6 shows the impact on *VV*, *HH*, and *VH* computed with the E and H spectra. There is only small difference between using different roughness spectra and the effect is strongest for *VH*. Over all, the foam modification of NRCS computation is only important in very high winds and can reach to about 2 dB; for wind speeds less than 20 m/s, the modification is less than about 0.25 dB, i.e., less than 6% difference.

2.4. Modification of the Roughness Spectrum

The H roughness model is constructed with the observed similarity relationship expressed as a power law between the dimensionless spectrum $B(k)$ and the dimensionless wind forcing parameter u_*/c as have been discussed in *Hwang and Wang* [2004] and *Hwang* [2005]

$$B\left(\frac{u_*}{c};k\right)=A(k)\left(\frac{u_*}{c}\right)^{a(k)}. \tag{8}$$

The parameters $A(k)$ and $a(k)$ are obtained from a free-drifting wave gauge (FDWG) system deployed in several field experiments conducted in the Gulf of Mexico. They can also be extracted from microwave radar and radiometer measurements, e.g., see the summary of the wind speed exponent $a(k)$ given in *Hwang* [1997] and *Trokhimovski and Irisov* [2000], as well as the radar spectrometer analysis of the roughness spectral components using Ku, C, and L band *VV* GMFs to derive both $A(k)$ and $a(k)$ as discussed in *Hwang et al*. [2013].

Figures 7a and 7b summarize the results from in situ and remote sensing measurements. The previous versions of the H roughness spectral model rely heavily on the in situ FDWG data. Figure 7a shows that the radar obtained $A(k)$ is generally lower than that from the FDWG in the C and L band region. Because $A(k)$ is proportional to the amplitude of the power-law function (8), the Bragg roughness is overestimated, as concluded in section 2.2.

The task of roughness model refinement involves the formulation of $A(k)$ and $a(k)$ incorporating, and placing more weight to, the remote sensing data. The details of the algorithm to compute the H roughness spectrum have been documented in *Hwang et al*. [2013, Appendix]. The only change in the present refinement is the fifth-order polynomial fitting functions of $A(k)$ and $a(k)$ for the middle branch $k_1 < k \le k_2$, with

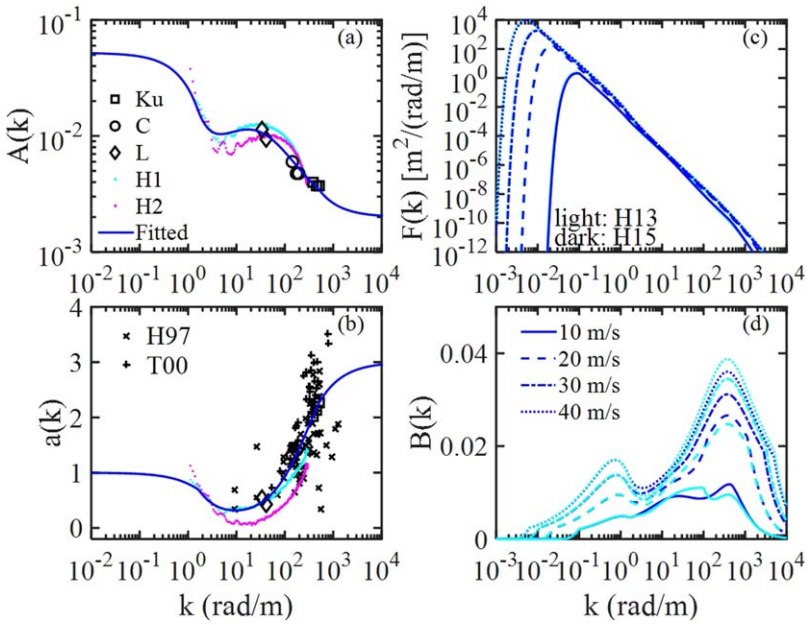

Figure 7. The data of (a) $A(k)$ and (b) $a(k)$, for the H spectral model combining both in situ oceanographic instruments and microwave remote sensors for refining the H roughness spectrum model; (c, d) are the modified 1-D displacement and dimensionless spectra (labeled H15). The modified spectra are compared with the version of *Hwang et al.* [2013]: H13.

the revised range of $k_1 = 1$ and $k_2 = 500$ rad/m. Using the notations $k_{ln} = \ln(k)$, $A_{ln} = \ln(A)$, and $a_{ln} = \ln(a)$, the polynomial fitting with greater weighting for the radar data produces

$$\begin{aligned} A_{ln} =& -1.6356\times10^{-3}k_{ln}^5 + 4.1084\times10^{-2}k_{ln}^4 - 3.6789\times10^{-1}k_{ln}^3 \\ &+ 1.3888k_{ln}^2 - 2.2193k_{ln} - 3.3179, \\ a_{ln} =& 1.4013\times10^{-3}k_{ln}^5 - 2.6997\times10^{-2}k_{ln}^4 + 1.5739\times10^{-1}k_{ln}^3 \\ &- 1.3020\times10^{-1}k_{ln}^2 - 7.5202\times10^{-1}k_{ln} + 2.3808\times10^{-2}. \end{aligned} \tag{9}$$

Figures 7c and 7d show the resulting 1-D displacement spectrum $F(k)$ and the dimensionless spectrum $B(k)$ computed for $U_{10} = 10$, 20, 30, and 40 m/s. The revised spectra (labeled H15) are compared with the version presented in *Hwang et al.* [2013] (labeled H13). Although the difference appears to be small, the impact on the NRCS computation is quite significant (section 3).

As have been done in *Hwang* [2008], *Hwang and Plant* [2010], and *Hwang et al.* [2013], we also made comparisons of the low-pass filtered mean square slopes (MSS) integrated from the revised spectrum with the field data obtained by an optical method (sun glitter analysis) [*Cox and Munk*, 1954] and Ka [*Walsh et al.*, 1998; *Vandemark et al.*, 2004], Ku [*Jackson et al.*, 1992], and C [*Hauser et al.*, 2008] band radars. The agreement remains comparable with the earlier versions because the band-passed integration quantity is not very sensitive to minor spectral modifications. Also, because the asymptotic functions toward both high and low wave numbers remain the same as those of H13, the integrated total MSS is bounded, as has been discussed in *Hwang et al.* [2013, section 5a].

3. Result

3.1. C Band

After implementing the modification of relative permittivity by air entrained by wave breaking and refinement of the surface roughness model incorporating the remote sensing results, the *VV* agreement with GMF improved for the H spectrum, especially in the low-wind portion (Figure 8). Over all, the ratio $\delta\sigma_{0VV}$ is mostly between −2 dB and +3 dB for wind speeds between 0 and 60 m/s, and incidence angles between 20 and 50°. For the E spectrum the *VV* ratio is between −1.5 and 4.5 dB. A side-by-side comparison with the baseline case has been presented in Figure 3.

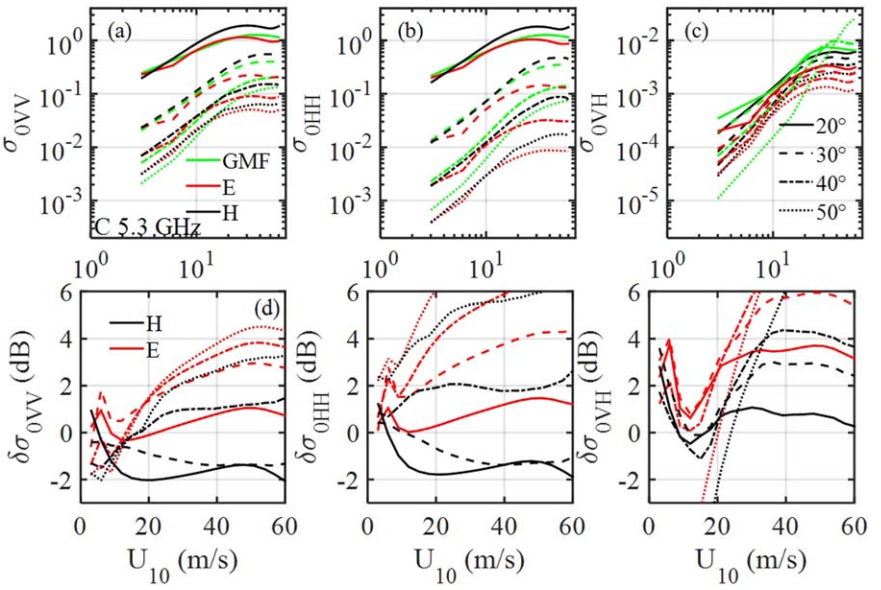

Figure 8. Comparison of C band GMFs and SSA2 solutions incorporating the modification of relative permittivity by foam, calculated with the E and H15 spectra: (a) *VV*, (b) *HH*, and (c) *VH*. The corresponding ratios GMF/SSA2 are shown in Figures 8d–8f.

Given the complex nature of the surface roughness produced by wind wave generation and breaking disturbances, it is unlikely that the relatively simple construction of the surface roughness spectrum models can be further improved significantly to achieve agreement much better than within ±3 dB over a wide range of wind speed, incidence angle, and microwave frequency. As a final step, the ratio of *VV*(*GMF*)/*VV*(*SSA*2), denoted as $\delta\sigma_{VVadj}$, is computed as an ad hoc correction of the surface roughness spectrum ($\delta\sigma_{VV}$ in Figure 8a is the $\delta\sigma_{VVadj}$ for CMOD5.n). The ratio is applied to the *HH* and *VH* SSA2 solutions, and the difference or ratio with the GMF gives the information of breaking contribution. The surface roughness and breaking contributions can then be separated from the polarimetric measurements. Rewriting (1) symbolically for the *VV*, *HH*, and *VH* NRCS as

$$\begin{aligned}
\sigma_{0VV}(f,\theta,U_{10}) &= G_{VV}(f,\theta,U_{10})B_{Radj}(k,U_{10}) \\
&= \sigma_{0RVV} = \sigma_{0VVGMF} \\
\sigma_{0HH}(f,\theta,U_{10}) &= G_{HH}(f,\theta,U_{10})\left[B_{Radj}(k,U_{10}) + B_{BHH}(k,U_{10})\right] \\
&= \sigma_{0RHH} + \Delta\sigma_{0HHadj} = \sigma_{0HHGMF} \\
\sigma_{0VH}(f,\theta,U_{10}) &= G_{VH}(f,\theta,U_{10})\left[B_{Radj}(k,U_{10}) + B_{BVH}(k,U_{10})\right] \\
&= \sigma_{0RVH} + \Delta\sigma_{0VHadj} = \sigma_{0VHGMF},
\end{aligned} \tag{10}$$

where subscript *adj* indicates that the roughness spectrum is adjusted so that the computed *VV* Bragg solution (σ_{0RVV}) matches the *VV* GMF, and the Δ quantity is the difference between *HH* or *VH* GMFs and the corresponding SSA2 solution of the Bragg contribution. Figure 9 displays the results of breaking contribution obtained from the co- and cross-polarization C band (5.3 GHz) GMFs discussed in section 2.2, showing a general quadratic to cubic wind speed dependence for $U_{10} < \sim$20–30 m/s (upper row).

The breaking contribution can also be expressed in terms of the equivalent roughness with reference to the Bragg surface roughness

$$\delta\sigma_{0pqadj} = \frac{\sigma_{0pqGMF}}{\sigma_{0Rpq}} = \frac{B_{Radj} + B_{Bpq}}{B_{Radj}}, \tag{11}$$

where subscript *pq* is *HH* or *VH*. The result is shown in dB scale in the bottom row of Figure 9. The relative weighting of the breaking contribution for the *HH* polarization depends strongly on the incidence angle. In contrast, the incidence angle dependence is less certain for the *VH* relative breaking contribution.

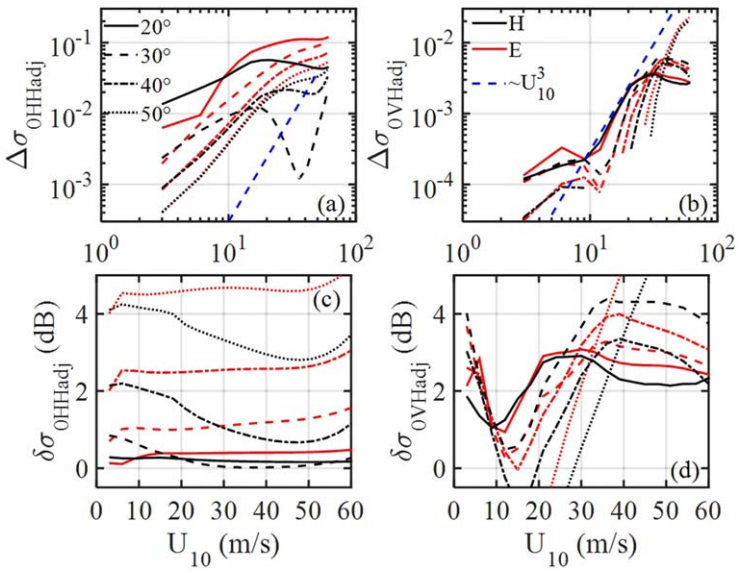

Figure 9. The final result of wave breaking contribution considering modification of relative permittivity by foam, refinement of roughness model and adjusting *VV* SSA2 solution to agree with the *VV* GMF. (left column) *HH*, (right column) *VH*; (top row) obtained from the difference GMF-SSA2, (bottom row) obtained from the ratio GMF/SSA2.

The *VH* signal level is notoriously low and frequently below the system noise level in low wind speeds and high incidence angles. Taking this factor into account, then the trend of $\delta\sigma_{0VHadj}$ for $U_{10} > \sim$10 m/s can be divided into two groups: prior- and post-signal saturation, and the incidence angle dependence in the two groups are reversed (Figure 9d). However, the issue of *VH* signal saturation remains unsettled. Refinement of the C band *VH* GMF in the future may provide a better estimation of the breaking contribution in *VH*.

With respect to the *HH* result, it is noted that the Envisat-ASAR and R2 quad-polarization database used to produce the C band *HH* GMF is restricted to θ between about 20 and 45° and wind speed less than about 20 m/s. The results extrapolated beyond the range should be treated with caution.

3.2. Ku and L Bands

Figure 10 shows the Ku band (14 GHz) results using the Ku2001 GMF. The Ku band GMF is available for *VV* and *HH* only. The top row shows the comparison of the GMF with the computed *VV* and *HH* NRCS using the E and H spectra over the range of 20–50° incidence angle and 3–60 m/s wind speed. The roughness adjustment factor $\delta\sigma_{VVadj}$ is mostly within $\pm$2 dB using the H spectrum and the range is slightly larger using the E spectrum (Figure 10c). The breaking contribution derived from comparing the GMF and SSA2 solutions are shown in Figures 10d (ratio) and 10e (difference). The results are similar to the C band computation but the wind speed dependence is somewhat steeper for the Ku band (compare Figures 9a and 10e).

Meissner et al. [2014] report L band (1.4 GHz) *VV*, *HH*, and *VH* NRCS data from the Aquarius satellite with wind speed coverage from 0 to 35 m/s and three incidence angles (29.4, 38.4, and 46.3°). Figures 11a–11c show the comparison between the SSA2 solutions and the Aquarius data. Both H and E spectral models perform quite well as indicated in the small values of $\delta\sigma_{VVadj}$ (Figure 11d). (Note the low-wind portion of the SSA2 solution is not very good because of the relatively coarse setup of the wave number vector representing the surface roughness spectrum in order to speed up the numerical computation, see discussions in section 4.2 on the comparison of CB and SSA2 solutions.) The breaking contribution expressed as an equivalent roughness (and given as the ratio $\delta\sigma$ and difference $\Delta\sigma$) is shown in Figures 11e and 11f for the *HH* polarization, and in Figures 11g and 11h for the *VH* polarization. Compared to the C and Ku band results (Figures 9 and 10), the magnitude of L band breaking contribution is smaller and its wind speed dependence is weaker.

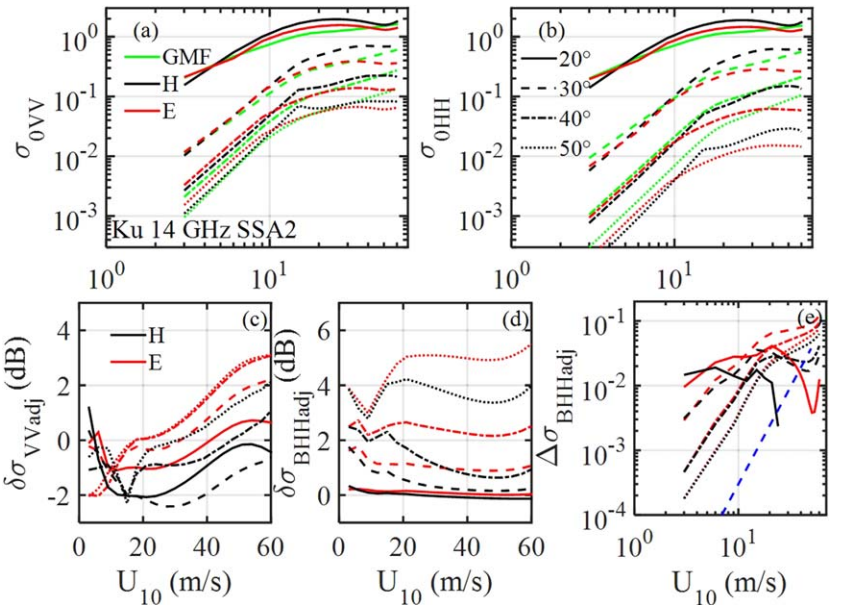

Figure 10. Comparison of Ku band GMF and SSA2 solutions calculated with the E and H15 spectra: (a) *VV* and (b) *HH*; (c) the *VV* adjustment factor GMF/SSA2, and the derived *HH* breaking wave contribution shown as (e) *HH* ratio GMF/SSA2 and (f) *HH* difference GMF-SSA2.

4. Discussion

4.1. Roughness and Breaking in Air-Sea Interaction

A very useful quantity of the ocean surface roughness for air-sea interaction applications is the band-pass-filtered mean square slope. For example, many studies have shown that the correlation between gas transfer velocity and ocean surface MSS integrated over some range of wave number k is considerably better than the correlation between gas transfer velocity and wind speed [e.g., *Bock et al*., 1999; *Frew et al*., 2004, 2007]. *Frew et al*. [2004] quantify the difference with field data: referenced to the wind speed correlation coefficient of about 0.77, the MSS correlation coefficient improvement ranges from 0.81 (k range 40–100 rad m^{-1}) to 0.92 (k range 400–800 rad m^{-1}). *Frew et al*. [2007] describe an application of dual-frequency (Ku and C band) spaceborne altimeter data for global estimation of air-sea gas transfer velocity fields. The

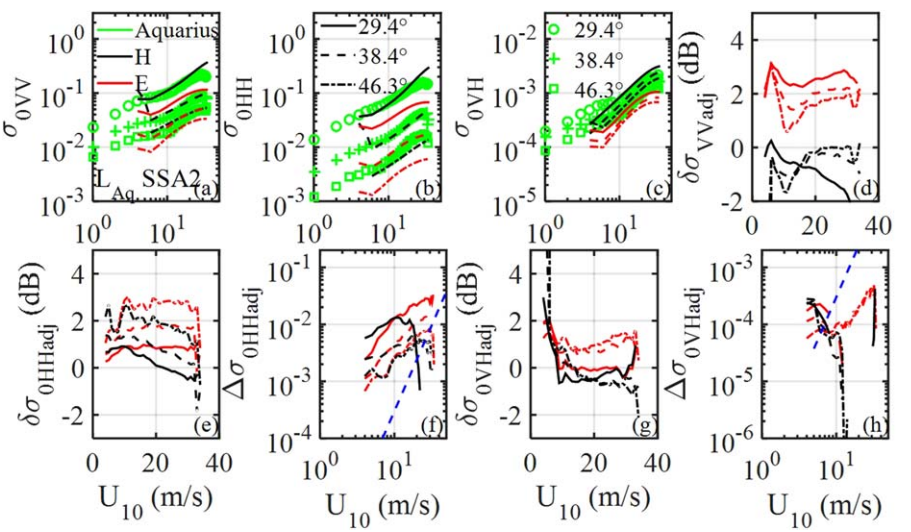

Figure 11. Comparison of L band Aquarius data and SSA2 solutions calculated with the E and H15 spectra: (a) *VV*, (b) *HH*, and (c) *VH*; (d) the *VV* adjustment factor GMF/SSA2; and the derived breaking wave contribution shown as (e) *HH* ratio GMF/SSA2, (f) *HH* difference GMF-SSA2, (g) *VH* ratio GMF/SSA2, and (h) *VH* difference GMF-SSA2.

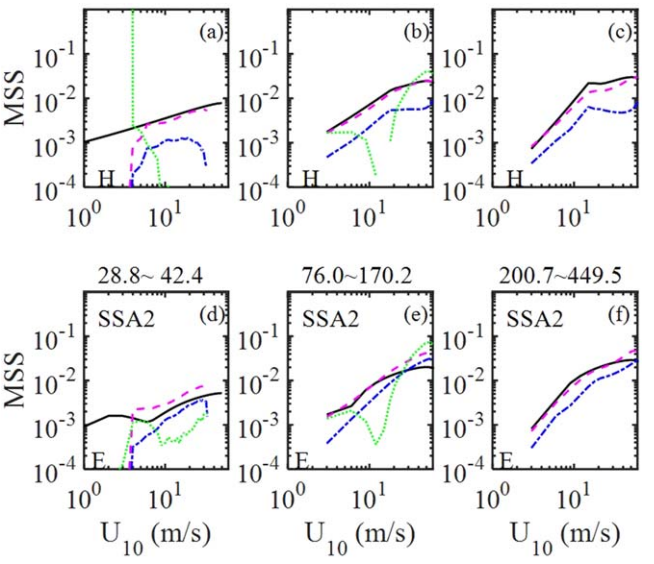

Figure 12. Mean square slopes integrated from spectral models (top row for H15 and bottom row for E) and radar backscattering: (a, d) L band, (b, e) C band, and (c, f) Ku band; both surface roughness and breaking equivalent roughness are presented. Curves labeled B_R, solid (black) lines, are from spectral model; B_{Radj}, dashed (magenta) lines, are from *VV* GMF; B_{BHH}, dashed-dotted (blue) lines, are *HH* breaking component; and B_{BVH}, dotted (green) lines, are *VH* breaking component. The range of integrated wave number is shown between the top and bottom figures for each microwave frequency.

relevance of small-scale surface roughness to air-sea interaction processes is also demonstrated in a recent publication reporting the improved correlation between the sea spray aerosol production and the roughness component of the microwave radiometer brightness temperature at 10.7 GHz (compared to the correlation with wind speed) [*Savelyev et al.*, 2014].

We can also use scatterometer or SAR to obtain the band-pass-filtered MSS. Figure 12 shows the wind speed relationship of the MSS integrated over the incidence angles of the L, C, and Ku band NRCS discussed in Figures 9–11, i.e., 29–46° for the L band, and 20–50° for the C and Ku bands. The top row (Figures 12a–12c) shows the results using the H spectrum, and the bottom row (Figures 12d–12f) shows the corresponding results using the E spectrum. The range of Bragg resonance wave number (in rad/m) for each frequency band is shown between the top and bottom figures. The solid $B_R(k)$ curve is based on the roughness spectral model and the dashed $B_{Radj}(k)$ curve is based on the *VV* GMF (10). The agreement between spectral models and radar observations is generally quite good. Based on the analysis of *Frew et al.* [2004] described at the beginning of this section, the MSS from Ku band frequency range is probably very useful for air-sea interaction studies.

The breaking contribution represented as an equivalent roughness is also integrated to get the equivalent MSS and shown in Figure 12 together with the surface roughness MSS. The dashed-dotted curve represents the *HH* result and the dotted curve for the *VH* result. The breaking contribution in radar backscattering is strongly dependent on the incidence angle and it is relatively weak for θ less than about 40°, as shown in Figures 9–11. For airborne, shipborne, land or tower-based radar systems, the incidence angle can be extended considerably toward grazing and the signal of breaking contribution would be much higher. The range of wave number coverage for a given radar frequency also expands with increased incidence angle coverage, as estimated by the Bragg resonance equation: $k_B = k_e 2\sin\theta$.

4.2. CB and SSA2 Solutions

The computation of SSA2 solution is very complex and time consuming since it requires the calculation of fourfold integrals with oscillating functions [*Fois et al.*, 2014]. For example, the results presented in this paper are typically computed for the incidence angle θ from 20 to 75° in 5° intervals and azimuth angle $\phi = 0$, 90, and 180°. For each wind speed, the computation time is about 81 min = 4860 s using a desktop personal computer (64 bit Windows 7 Operating System, 2.80 GHz Intel® processor with 32 GB installed memory). For each microwave frequency it takes about 26 h to complete a series of wind speed $U_{10} = 3$–60 m/s in 3 m/s steps. In comparison, for the same configuration the computation time of the CB solution is about 6 s for one wind speed, and 120 s for the wind speed series of each microwave frequency. Given the great disparity of the computation cost between the two solutions (~800:1), it is worthwhile to investigate the relative merit of the costs and trade-offs.

As discussed in section 3.2 regarding the L band computations, the SSA2 solution uses a coarse wave number vector to represent the surface roughness spectrum (256 log-spaced elements to cover the k range between $2\pi/376$ rad/m and $5k_e$). As a consequence, the computed results for low winds are not very good.

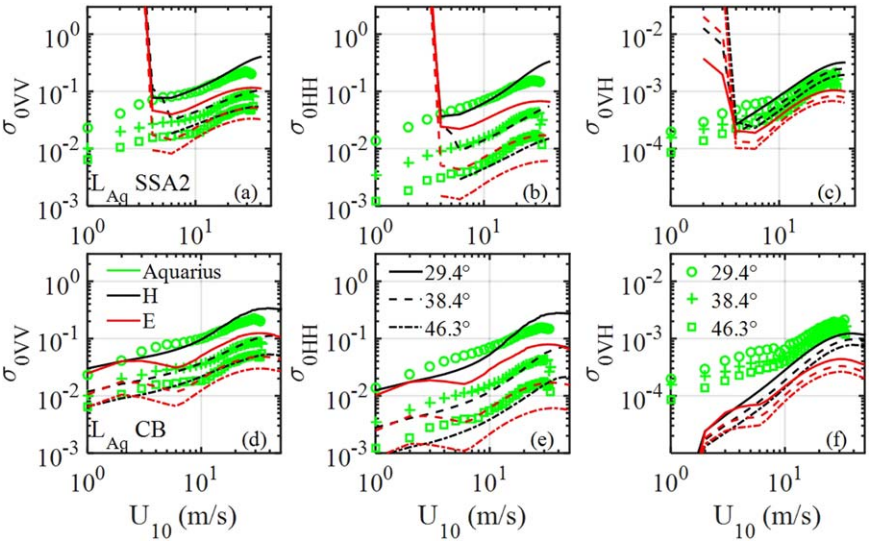

Figure 13. Comparison of the (top row) SSA2 and (bottom row) CB solutions calculated with the E and H15 spectra for the L band Aquarius data: (a, d) *VV*, (b, e) *HH*, and (c, f) *VH*.

The CB solution is computed on the integrated upwind and crosswind low-passed mean square slopes and the Bragg resonance component of the wave spectrum. The dependence on the spectral wave number resolution is less severe than the SSA2 solution. The CB solution discussed in this paper in fact uses a coarser wave number grid than the SSA2 solution—141 log-spaced elements covering the range $10^{-3}-10^{4}$ rad/m. The SSA2 and CB solutions for the Aquarius L band are compared in Figure 13. The problem of the low wind region in the SSA2 solution disappears in the CB solution as a consequence of decreased dependence on the wave number resolution for representing the roughness spectrum.

Figure 14 shows the computational results of SSA2 and CB solutions for the C band frequency; the GMF is superimposed for reference; the top row is computed with the H spectrum and the bottom row with the E spectrum. Generally, there are only small differences between the SSA2 and CB solutions in the copolarization (*VV* and *HH*) computations using the E spectrum, but up to 2 dB difference is found in the low incidence angles ($\theta < \sim 30°$) and high winds ($U_{10} > \sim 20$ m/s) using the H spectrum. The exact cause

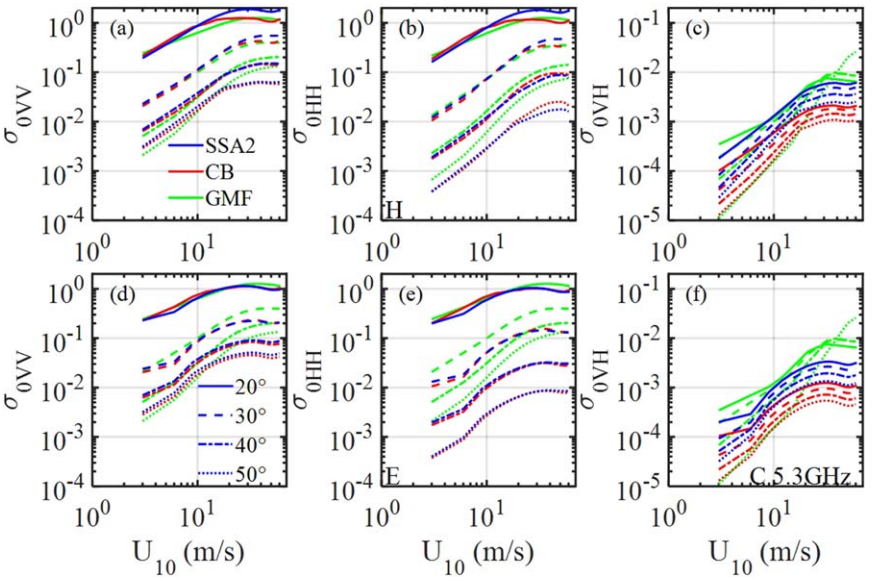

Figure 14. Comparison of the C band SSA2 and CB solutions, the GMFs are also plotted for reference. The computation with the (top row) H15 spectrum and (bottom row) E spectrum: (a, d) *VV*, (b, e) *HH*, and (c, f) *VH*.

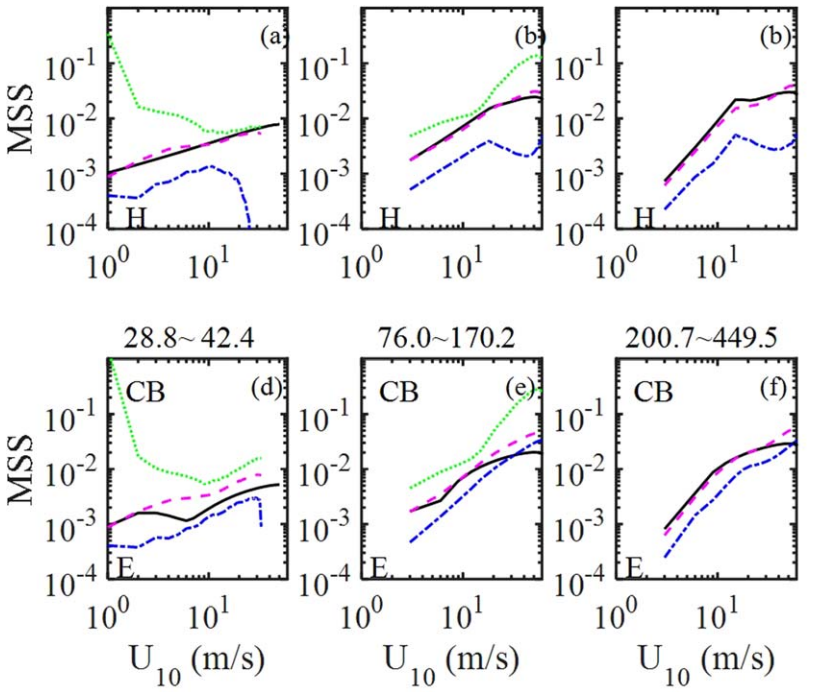

Figure 15. Same as Figure 12 but the results are based on the CB solution.

is unknown at this stage. There is significant underestimation of the CB solution for the cross polarization (*VH*), which has been pointed out by *Voronovich and Zavorotny* [2011, 2014] as caused by the importance of the second-order Bragg scattering for the *VH*. The SSA2 solution includes the first and second-order Bragg components whereas the CB solution only accounts for the first-order Bragg component.

The agreement between the Bragg solutions (SSA2 and CB) with the GMF is generally quite good for *VV*. Differences between the Bragg solutions (SSA2 and CB) with the *HH* and *VH* GMFs are used to extract the breaking information. Applying the analysis procedure of separating the surface roughness and wave breaking contributions described in section 3.1 to the CB solution, the MSS of surface roughness and equivalent breaking roughness based on the copolarization calculations are basically the same as those obtained from the SSA2 solutions (compare Figures 12 and 15). The CB calculated cross-polarization breaking equivalent roughness is much higher, reflecting the underestimation of the CB solution for the cross-polarization returns.

Figure 16 shows the ratio $\delta\sigma_{0VHadj}$ (11), which represents the *VH* wave breaking equivalent roughness with reference to the Bragg roughness. The results are computed for the two-frequency bands with cross-polarization GMFs available: C and L from R2 and Aquarius, respectively. The CB solution (darker curves) is about 3–4 dB (2–2.5 times) higher than that of the SSA2 solution (lighter curves); the level of CB underestimation differs only slightly between the E and H roughness spectra. We can apply this result to enhance the surface roughness spectrum by the $\delta\sigma_{0VHadj}$ factor in cross-polarization computation using the CB solution and take advantage of the 800:1 computation time saving.

Figure 17 shows the ratio $\delta\sigma_{0HHadj}$, which represents the *HH* wave breaking equivalent roughness with reference to the Bragg roughness. The results are computed for Ku, C, and L bands. The difference between the SSA2 and CB solutions is relatively small using the E spectra but may differ by as much as 2 dB toward high incidence angle using the H spectrum. The breaking contribution is significantly smaller in L band than in C and Ku bands.

Figure 18 shows the ratio $\delta\sigma_{0VVadj}$. This quantity [*VV*(GMF)/*VV*(SSA2) or *VV*(GMF)/*VV*(CB)] is useful for evaluating the roughness spectral models because the *VV* is dominated by the Bragg resonance scattering: the closer of this ratio to 1.0 (0 dB) the better agreement of the Bragg solution to the *VV* GMF. The Bragg

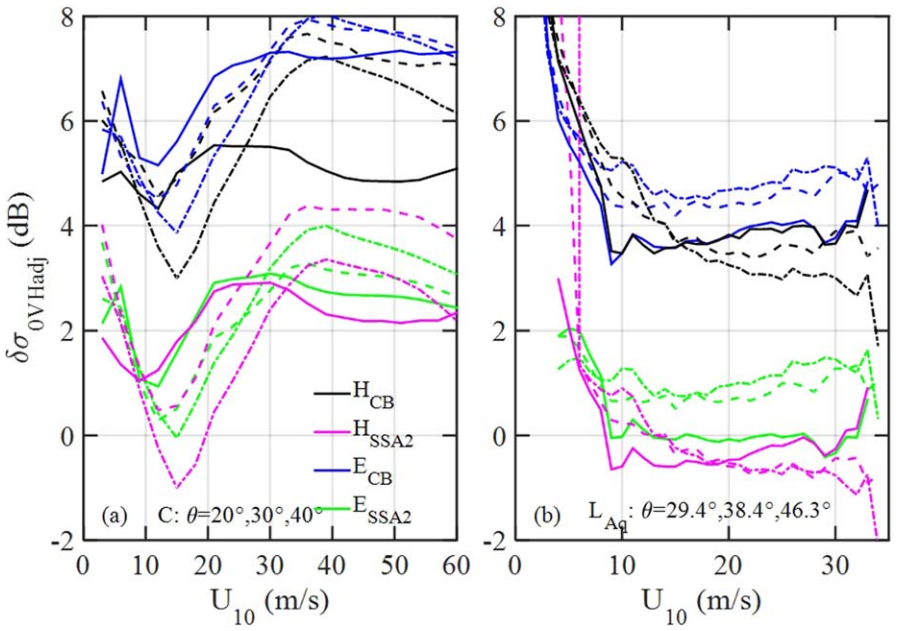

Figure 16. The difference between the CB and SSA2 solutions of the *VH* breaking contributions in terms of the ratio GMF/CB and GMF/SSA2, (a) C band and (b) L band. Results for using the E and H spectra are identified in the legend.

solutions calculated with the modified H spectrum described in section 2.4 yield the range of $\delta\sigma_{0VVadj}$ mostly within -2 to $+3$ dB over the range of wind speeds between 3 and 60 m/s, and incidence angles between 20 and 50° for the three-frequency bands (Ku, C, and L) we have evaluated. The E spectrum also performs well but with somewhat larger differences with the GMFs.

4.3. Other Issues

In this paper, we describe a method to extract the ocean surface roughness and small-scale wave breaking information from the radar backscattering in different polarizations. There are three components in the

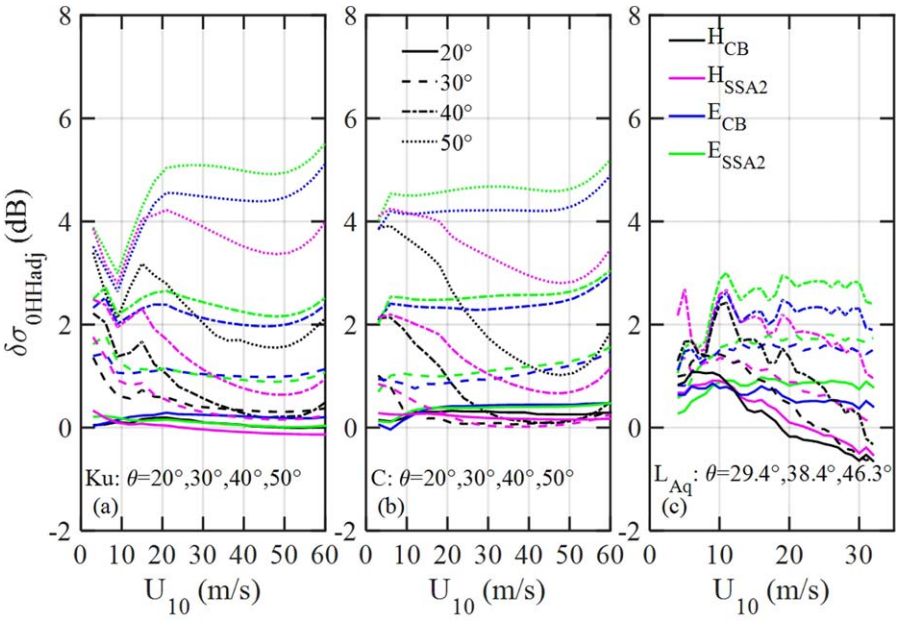

Figure 17. The difference between the CB and SSA2 solutions of the *HH* breaking contributions in terms of the ratio GMF/CB and GMF/SSA2, (a) Ku band, (b) C band, and (c) L band. Results for using the E and H spectra are identified in the legend.

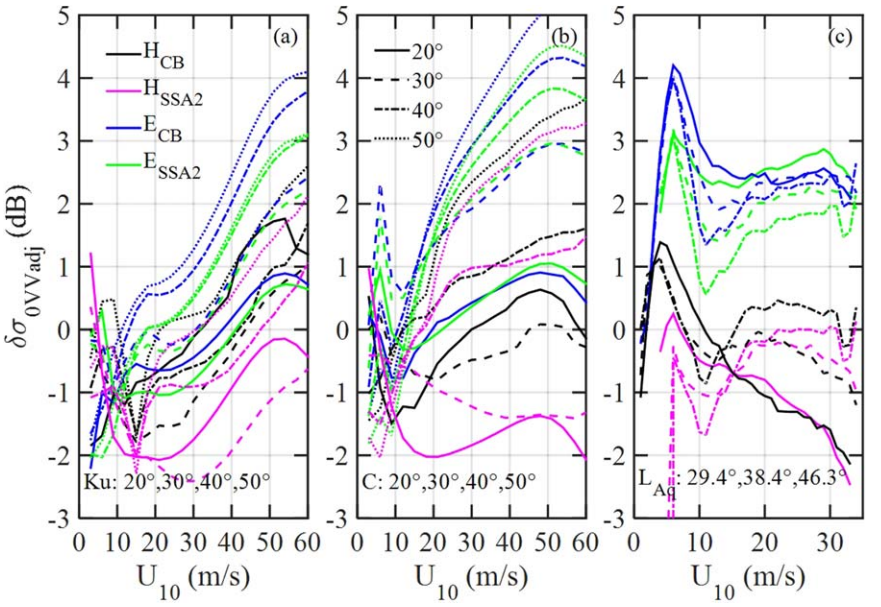

Figure 18. The difference between the CB and SSA2 *VV* solutions in terms of the ratio GMF/CB and GMF/SSA2, (a) Ku band, (b) C band, and (c) L band. Results for using the E and H spectra are identified in the legend.

computational procedure: electromagnetic (EM) scattering models, NRCS measurements, and surface roughness spectrum models. Of the three, the component of the surface roughness spectrum models is the weakest link. This is the main reason that although the EM theory of microwave scattering from roughness surfaces is well researched, operational algorithms rely on empirical relations established from correlating collocated and simultaneous data sets of in situ wind speeds and backscattering cross sections, rather than relying on theoretical models. An extended discussion has been presented in *Hwang et al*. [2002].

We hope to narrow this gap by making use of the good quality of theoretical models and NRCS measurements to improve the ocean surface roughness models. "Calibrated" with the *VV* GMF, the H spectrum is now generally within about -2 to $+3$ dB accuracy. The ratio between *VV* GMF and model solution can be applied to the H spectrum to obtain the ocean surface roughness spectrum "as the radar sees it." The adjusted roughness spectrum is then used for computing the Bragg component of the *HH* and *VH* NRCS. The difference from the *HH* and *VH* GMFs can then provide useful information about the small-scale wave breaking properties.

We emphasize that such level of the error of analytical computation (caused mainly by the roughness models) is still far from useful for improving operational applications of wind retrieval using radar backscattering. For an illustration, Figure 19 shows an example of the analytical computation errors expressed in terms of $\delta\sigma_0$ and the inaccuracy of retrieved wind speed ΔU_{10}. The error of a fractional dB in NRCS can translate to a rather large wind speed error in high winds where the gradient $dU_{10}/d\sigma_0$ is rather large, reaching infinity in case of signal saturation. The advance we are seeking to achieve is the improvement of ocean surface properties (the

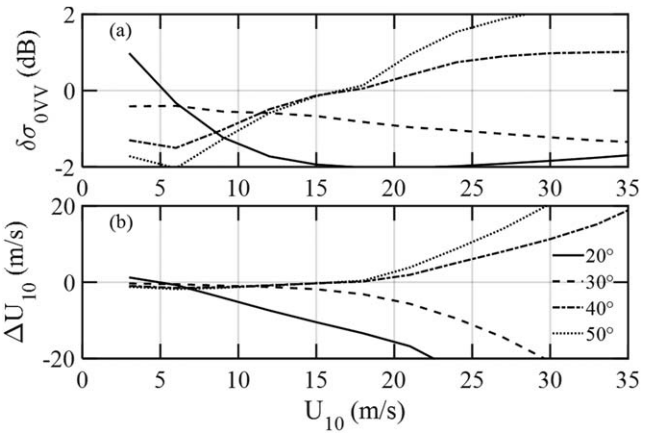

Figure 19. Errors of model computations in terms of (a) $\delta\sigma$ and (b) ΔU_{10}. The example given is the SSA2 *VV* solutions using the H15 roughness spectrum compared to CMOD5.n.

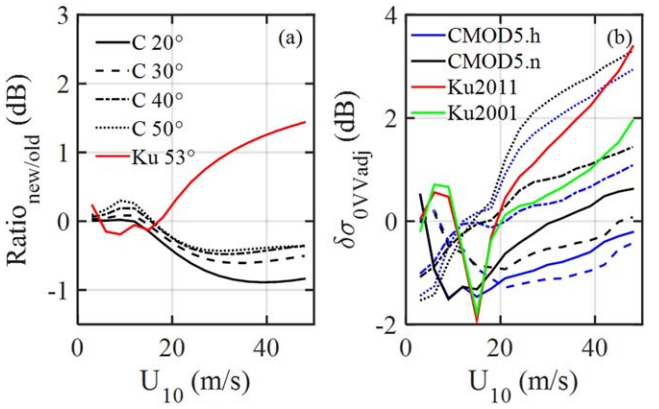

Figure 20. Comparison of CMOD5.h versus CMOD5.n and KU2011 versus Ku2001 (*VV*): (a) the ratios CMOD5.h/CMOD5.n and Ku2011/Ku2001; and (b) $\delta\sigma_{0VVadj}(U_{10})$ (CB solution, H15 spectrum).

weakest link) using radar backscattering coupled with analytical EM models.

With regards to the GMFs, there are continuous efforts to improve the performance especially for the high-wind conditions. CMOD5.h [*Soisuvarn et al.*, 2013] and Ku2011 [*Ricciardulli and Wentz*, 2011; *Ricciardulli et al.*, 2012] have shown considerable improvement in the high-wind region compared to CMOD5.n and Ku2001, respectively. Figure 20a shows the ratio between the new and old GMFs. For U_{10} less than about 20 m/s, the ratio is generally smaller than about 0.3 dB, but can grow to about −1 to 1.5 dB at high winds (the CMOD5.h is given in lookup tables with 50 m/s maximum wind speed). We can use this ratio to revise the computations presented in the last two sections. An example for $\delta\sigma_{0VVadj}$ (referenced to the H15 spectral model and CB solution) is shown in Figure 20b. The black curves are the results using the CMOD5.n, i.e., identical to the black curves in Figure 18b; the blue curves are the revision with reference to CMOD5.h. The same procedure can be applied to the *HH* and *VH* computations. Note that Ku2011 is given for one incident angle of each polarization (46° for HH and 53° for VV). Because of the different incidence angles, we are not able to take advantage of the Ku improvement for the roughness and breaking analysis described in this paper.

5. Summary

Microwave backscattering from the sea surface contains valuable information of the ocean surface roughness and wave breaking that is very difficult to measure using conventional oceanographic instruments. Making use of the property that *VV*, *HH*, and *VH* respond to roughness and breaking differently, a method to extract the quantitative roughness and breaking properties is outlined. Basically, the GMFs established from global NRCS measurements are treated as field data of roughness and wave breaking reflected in the interaction of microwave and the sea surface. Theoretical solutions of the Bragg resonance scattering from the surface roughness contributions for *VV*, *HH*, and *VH* are computed using the SSA2 and CB solutions. The *VV* comparison between the GMF and Bragg solutions is useful for refining the ocean surface roughness spectral model. Once a satisfactory roughness model is obtained, the differences between the GMF and SSA2 solutions is used to derive the information of small-scale surface wave breaking properties. The information is useful for microwave applications as well as air-sea interaction research in areas such as gas transfer and sea spray aerosol production. We emphasize that the results regarding the dependence on frequency, incidence angle, and wind speed as presented in this paper are based on the still-evolving GMFs and roughness models. We expect further refinement in the future with improved accuracy of the surface roughness models and GMFs. This assessment is based on the best information available at this stage.

Acknowledgments

This work was sponsored by the Office of Naval Research (NRL program elements 61153N). We are grateful for the comments from two anonymous reviewers and the help by Seubson Soisuvarn (NOAA) for the lookup tables of CMOD5.h and CMOD5.n GMFs. We are grateful for the comments and suggestions from two anonymous reviewers. One of them pointed out that CMOD5.h and Ku2011 have significantly improvement in the high wind retrieval. NRL publication: NRL/JA/7260-15-0026. All the GMFs and data used in this paper have been published in the referenced papers. Data and processing codes can also be obtained from contacting the corresponding author at paul.hwang@nrl.navy.mil.

References

Anguelova, M. D. (2008), Complex dielectric constant of sea foam at microwave frequencies, *J. Geophys. Res.*, *113*, C08001, doi:10.1029/2007JC004212.

Bock, E. J., T. Hara, N. M. Frew, and W. R. McGillis (1999), Relationship between air-sea gas transfer and short wind waves, *J. Geophys. Res.*, *104*, 25,821–25,831.

Callaghan, A., G. de Leeuw, L. Cohen, and C. D. O'Dowd (2008), Relationship of oceanic whitecap coverage to wind speed and wind history, *Geophys. Res. Lett.*, *35*, L23609, doi:10.1029/2008GL036165.

Cox, C. S., and W. Munk (1954), Statistics of the sea surface derived from sun glitter, *J. Mar. Res.*, *13*, 198–227.

Elfouhaily, T., B. Chapron, K. Katsaros, and D. Vandemark (1997), A unified directional spectrum for long and short wind-driven waves, *J. Geophys. Res.*, *102*, 15,781–15,796.

Fois, F., P. Hoogeboom, F. Le Chevalier, and A. Stoffelen (2014), Future ocean scatterometry at very strong winds, in *IEEE International Geoscience and Remote Sensing Symposium*, pp. 3886–3889, IEEE, IGASS2014: Quebec, Canada.

Frew, N. M., et al. (2004), Air-sea gas transfer: Its dependence on wind stress, small-scale roughness, and surface films, *J. Geophys. Res.*, *109*, C08S17, doi:10.1029/2003JC002131.
Frew, N. M., D. M. Glover, E. J. Bock, and S. J. McCue (2007), A new approach to estimation of global air-sea gas transfer velocity fields using dual-frequency altimeter backscatter, *J. Geophys. Res.*, *112*, C11003, doi:10.1029/2006JC003819.
Hauser, D., G. Caudal, S. Guimbard, and A. A. Mouche (2008), A study of the slope probability density function of the ocean waves from radar observations, *J. Geophys. Res.*, *113*, C02006, doi:10.1029/2007JC004264.
Hersbach, H., A. Stoffelen, and S. de Haan (2007), An improved C-band scatterometer ocean geophysical model function: CMOD5, *J. Geophys. Res.*, *112*, C03006, doi:10.1029/2006JC003743.
Hwang, P. A. (1997), A study of the wavenumber spectra of short water waves in the ocean. Part 2: Spectral model and mean square slope, *J. Atmos. Oceanic Technol.*, *14*, 1174–1186.
Hwang, P. A. (2005), Wave number spectrum and mean-square slope of intermediate-scale ocean surface waves, *J. Geophys. Res.*, *110*, C10029, doi:10.1029/2005JC003002.
Hwang, P. A. (2008), Observations of swell influence on ocean surface roughness, *J. Geophys. Res.*, *113*, C12024, doi:10.1029/2008JC005075.
Hwang, P. A. (2012), Foam and roughness effects on passive microwave remote sensing of the ocean, *IEEE Trans. Geosci. Remote Sens.*, *50*, 2978–2985.
Hwang, P. A. and W. J. Plant (2010), An analysis of the effects of swell and roughness spectra on microwave backscatter from the ocean, *J. Geophys. Res.*, *115*, C04014, doi:10.1029/2009JC005558.
Hwang, P. A. and D. W. Wang (2004), An empirical investigation of source term balance of small scale surface waves, *Geophys. Res. Lett.*, *31*, L15301, doi:10.1029/2004GL020080.
Hwang, P. A., Y.-H. L. Hsu and J. Wu (1990), Air bubbles produced by breaking wind waves: A laboratory study, *J. Phys. Oceanogr.*, *20*, 19–28.
Hwang, P. A., D. W. Wang, W. J. Teague, G. A. Jacobs, J. Wesson, D. Burrage, and J. Miller (2002), Anatomy of the ocean surface roughness, *NRL Formal Rep. NRL/FR/7330-02-10036*, 45 pp., Naval Research Laboratory, Washington D. C.
Hwang, P. A., B. Zhang, J. V. Toporkov, and W. Perrie (2010), Comparison of composite Bragg theory and quad-polarization radar backscatter from RADARSAT-2: With applications to wave breaking and high wind retrieval, *J. Geophys. Res.*, *115*, C08019, doi:10.1029/2009JC005995.
Hwang, P. A., D. M. Burrage, D. W. Wang, and J. C. Wesson (2013), Ocean surface roughness spectrum in high wind condition for microwave backscatter and emission computations, *J. Atmos. Oceanic Technol.*, *30*, 2168–2188.
Hwang, P. A., A. Stoffelen, G.-J. van Zadelhoff, W. Perrie, B. Zhang, H. Li, and H. Shen (2015), Cross polarization geophysical model function for C-band radar backscattering from the ocean surface and wind speed retrieval, *J. Geophys. Res. Oceans*, *120*, 893–909, doi:10.1029/2014JC010439.
Jackson, F. C., W. T. Walton, D. E. Hines, B. A. Walter, and C. Y. Peng (1992), Sea surface mean-square slope from K_u-band backscatter data, *J. Geophys. Res.*, *97*, 11,411–11,427.
Meissner, T., and F. J. Wentz (2009), Wind-vector retrievals under rain with passive satellite microwave radiometers, *IEEE Trans. Geosci. Rem. Sens.*, *47*, 3065–3083.
Meissner, T., F. J. Wentz, and L. Ricciardulli (2014), The emission and scattering of L-band microwave radiation from rough ocean surfaces and wind speed measurements from the Aquarius sensor, *J. Geophys. Res. Oceans*, *119*, 6499–6522, doi:10.1002/2014JC009837.
Mouche, A. A., D. Hauser, J. Daloze, and C. Guerin (2005), Dual-polarization measurements at C-band over the ocean: Results from airborne radar observations and comparison with ENVISAT ASAR data, *IEEE Trans. Geosci. Remote Sens.*, *43*, 753–769.
Plant, W. J. (1990), Bragg scattering of electromagnetic waves from the air-sea interface, in *Surface Waves and Fluxes*, vol. II, edited by G. L. Geernaert and W. L. Plant, pp. 41–108. Kluwer Acad. Publ., Springer, Netherlands.
Ricciardulli, L., and F. Wentz (2011), Reprocessed QuikSCAT (V04) wind vectors with Ku-2011 geophysical model function, *Tech. Rep. 043011*, 8 pp., Remote Sens. Syst., Santa Rosa, Calif.
Ricciardulli, L., T. Meissner, and F. Wentz (2012), Towards a climate data record of satellite ocean vector winds, in *IEEE International Geoscience and Remote Sensing Symposium*, pp. 2067–2069, IEEE, IGASS2012: Munich, Germany.
Savelyev, I. B., M. D. Anguelova, G. M. Frick, D. J. Dowgiallo, P. A. Hwang, P. F. Caffrey, and J. P. Bobak (2014), On direct passive microwave remote sensing of sea spray aerosol production, *Atmos. Chem. Phys.*, *14*, 11,611–11,631.
Soisuvarn, S., Z. Jelenak, P. S. Chang, S. O. Alsweiss, and Q. Zhu (2013), CMOD5.H—A high wind geophysical model function for C-band vertically polarized satellite scatterometer measurements, *IEEE Trans. Geosci. Remote Sens.*, *50*, 3744–3760.
Stogryn, A. (1972), The emissivity of sea foam at microwave frequencies, *J. Geophys. Res.*, *77*, 1658–1666.
Trokhimovski, Y. G., and V. G. Irisov (2000), The analysis of wind exponents retrieved from microwave radar and radiometric measurements, *IEEE Trans. Geosci. Remote Sens.*, *38*, 470–479.
Valenzuela, G. R. (1978), Theories for the interaction of electromagnetic and oceanic waves—A review, *Boundary Layer Meteorol.*, *13*, 61–85.
van Zadelhoff, G.-J., A. Stoffelen, P. W. Vachon, J. Wolfe, J. Horstmann, and M. Belmonte Rivas (2014), Retrieving hurricane wind speeds using cross polarization C-band measurements, *Atmos. Meas. Tech.*, *7*, 437–449.
Vandemark, D., B. Chapron, J. Sun, G. H. Crescenti, and H. C. Graber (2004), Ocean wave slope observations using radar backscatter and laser altimeters, *J. Phys. Oceanogr.*, *34*, 2825–2842.
Verspeek, J., A. Stoffelen, M. Portabella, H. Bonekamp, C. Anderson, and J. F. Saldana (2010), Validation and calibration of ASCAT using CMOD5.n, *IEEE Trans. Geosci. Remote Sens.*, *48*, 386–395.
Voronovich, A. G. (1994), Small-slope approximation for electromagnetic wave scattering at a rough interface of two dielectric half-spaces, *Waves Random Media*, *4*, 337–367.
Voronovich, A. G., and V. U. Zavorotny (2011), Depolarization of microwave backscattering from a rough sea surface: Modeling with small-slope approximation, in *IEEE International Geoscience and Remote Sensing Symposium*, pp. 2003–2036, IEEE, IGASS2011, Vancouver, Canada.
Voronovich, A. G., and V. U. Zavorotny (2014), Full-polarization modeling of monostatic and bistatic radar scattering from a rough sea surface, *IEEE Trans. Antennas Propag.*, *62*, 1363–1371.
Walsh, E. J., D. C. Vandemark, C. A. Friehe, S. P. Burns, D. Khelif, R. N. Swift, and J. F. Scott (1998), Measuring sea surface mean square slope with a 36-GHz scanning radar altimeter, *J. Geophys. Res.*, *103*, 12,587–12,601.
Wright, J. W. (1966), Backscattering from capillary waves with application to sea clutter, *IEEE Trans. Antennas Propag.*, *14*, 749–754.
Wright, J. W. (1968), A new model for sea clutter, *IEEE Trans. Antennas Propag.*, *16*, 217–223.
Wu, J. (1981), Bubble populations and spectra in near-surface ocean: Summary and review of field measurements, *J. Geophys. Res.*, *86*, 457–463.
Zhang, B., W. Perrie, P. Vachon, J. A. Zhang, E. W. Uhlhorn, and Y. He (2014), High resolution hurricane vector winds from C-band dual-polarization SAR observations., *J. Atmos. Oceanic Tech.*, *31*, 272–286.